mater.scichina.com link.springer.com
Published online 21 July 2022 | https://doi.org/10.1007/s40843-022-2119-1
Sci China Mater 2023, 66(1): 193–201

Si-CMOS-compatible 2D $PtSe_2$-based self-driven photodetector with ultrahigh responsivity and specific detectivity

Peng Ye, Han Xiao, Qinghai Zhu, Yuhan Kong, Youmei Tang and Mingsheng Xu*

ABSTRACT Photodetectors (PDs) based on two-dimensional (2D) materials are attracting considerable research interest due to the unique properties of 2D materials and their tunable spectral response. However, their performance is not outstanding enough, and the compatibility of their fabrication process with Si-complementary metal oxide semiconductor (CMOS) process flow needs evaluation. Here, we report an unprecedented high-performance, air-stable, self-driven, and broadband room-temperature PD based on the architecture of the $PtSe_2$/ultrathin SiO_2/Si heterojunction. The PD exhibits a very prominent responsivity of 8.06 A W^{-1}, a truly high specific detectivity of 4.78×10^{13} cm $Hz^{1/2}$ W^{-1}, an extremely low dark current of 0.12 pA, and a fantastic photocurrent/dark current ratio of 1.29×10^9 at zero bias. The measured photocurrent responsivities at wavelengths of 375, 532, 1342, and 1550 nm are 2.12, 5.56, 18.12, and 0.65 mA W^{-1}, respectively. Moreover, the fabricated 9×9 device array not only illustrates the very high uniformity and reproducibility of the PDs but also shows great potential in the field of ultraviolet-visible-near infrared illumination imaging applications with a fabrication fully compatible with Si-CMOS technologies. Our design of the $PtSe_2$/ultrathin SiO_2/Si heterojunction PD greatly suppresses dark current, improves the diode ideality factor, and increases the potential barrier. Accordingly, it paves the way for a general strategy to enhance the performance of PDs used in novel optoelectronic applications.

Keywords: two-dimensional materials, $PtSe_2$, Si-based photodetector, self-driven photodetector

INTRODUCTION

A p–n junction is a popular and simple architecture for developing high-performance photodetectors (PDs) [1–3]. An interface with a suitable passivation layer can greatly reduce the recombination of carriers at the interface, which is beneficial for suppressing the dark current [4,5]. To solve the shortcomings of traditional PDs, such as the complex preparation process, narrow detection range, high cost, and strict working environment [6–8], PDs based on two-dimensional (2D) materials, such as graphene and transition metal dichalcogenides (TMDs), have been extensively explored due to their excellent optical and electrical properties, such as a tunable bandgap, strong interaction with light, and good mechanical flexibility [9–12]. Moreover, whether or not the fabrication of functional devices with 2D materials (2D-Mat) is compatible with the Si-complementary metal oxide semiconductor (CMOS) process flow is essential for their incorporation into current Si-CMOS technologies [13]. Thus, 2D-Mat/Si heterostructure PDs are attracting considerable interest.

Among TMDs, 2D platinum diselenide ($PtSe_2$) was reported to have a high carrier mobility and tunable bandgap in the range of approximately 0–1.2 eV, dependent upon its layer numbers [14,15]. Furthermore, $PtSe_2$ is environmentally friendly and stable, and its synthesis temperature is compatible with silicon-based technology, which makes it a potential candidate for Si-based optoelectronics [16]. The tunable and narrow bandgap of $PtSe_2$ films brings opportunities for broadband detection from near-infrared (NIR) to midinfrared (MIR) bands [17]. Hence, $PtSe_2$-based heterostructures, such as $PtSe_2$/Si, $PtSe_2$/CdTe, and $PtSe_2$/GaAs PDs, have been reported [18–21]. However, despite these efforts, PDs based on $PtSe_2$ and other 2D materials still suffer from an insufficient rectification ratio, small I_{light}/I_{dark} ratio (where I_{light} refers to the photocurrent, and I_{dark} refers to the dark current), low responsivity, low specific detectivity, and large dark current, which severely limits their potential for commercial applications.

Here, we report a room-temperature high-performance self-driven PD based on a $PtSe_2$/ultrathin SiO_2/Si structure. The introduction of ultrathin SiO_2 as a dielectric layer to separate the $PtSe_2$ from the Si increases the interface barrier height but without influence on the bipolar carrier transport and passivates the Si surface. I_{dark} at zero bias, rectification ratio within ±5 V, and ideality factor (n) of the PD at room temperature in the dark are 0.12 pA, 5.7×10^7, and 1.015, respectively. Through the design of ultrathin SiO_2, the PDs fully utilize carriers photogenerated by the Si and $PtSe_2$ films. Under 808-nm NIR illumination at zero bias, the PD has a large I_{light}/I_{dark} ratio of ~1.29×10^9, a decent responsivity of 8.06 A W^{-1}, a truly specific detectivity (D_M^*) of 4.78×10^{13} Jones (1 Jones = 1 cm $Hz^{1/2}$ W^{-1}), and a fast response speed of 14.1/15.4 µs. Our PD with D_M^* larger than 3.85×10^9 Jones has a strong responsivity of 2.12, 5.56, and 0.65 mA W^{-1} under ultraviolet (UV, 375 nm), visible (Vis, 532 nm), and NIR (1550 nm) illuminations, respectively. The potential of the UV-Vis-NIR illumination imaging application is demonstrated by fabricating a 9×9 device array with very high homogeneity and reproducibility and compatibility with Si-CMOS technologies.

School of Micro-Nano Electronics, State Key Laboratory of Silicon Materials, Zhejiang University, Hangzhou 310027, China
* Corresponding author (email: msxu@zju.edu.cn)

© Science China Press and Springer-Verlag GmbH Germany, part of Springer Nature 2022

EXPERIMENTAL SECTION

Material synthesis

In this work, a multilayered $PtSe_2$ film was prepared by the thermally assisted conversion (TAC) technique. In brief, a platinum (Pt) layer was first-deposited on the as-prepared SiO_2/Si (~3 nm SiO_2 thickness) substrate using a magnetron sputtering system. Before deposition, the wafer was carefully cleaned according to standard cleaning techniques to remove ions and organic impurities. Then, the Pt-deposited substrate was transferred to the downstream side of a chemical vapor deposition furnace, while selenium (Se) powder (99.99% purity) was loaded at the upstream side. The Se powder was evaporated at 222°C, and the evaporated Se was transported to the Pt-deposited substrate under 50 sccm (standard cubic centimeters per minute) of a fixed Ar/H_2 (9:1) flow. The temperature of the downstream side was set to 400°C and kept for 2 h to ensure a complete selenization, followed by natural cooling to room temperature.

Preparation of the device

To construct the $PtSe_2$/ultrathin SiO_2/Si heterojunction-based PD, a window (0.05 cm × 0.05 cm) was defined on the planar SiO_2/n-Si (285 nm SiO_2) substrate *via* traditional lithography, followed by removing the SiO_2 insulating layer within the window *via* a buffered oxide etching (BOE) process. Afterward, the prepared substrate was exposed to a clean room ambient for the natural formation of a ~3-nm SiO_2 insulating layer on the Si. The $PtSe_2$ film was directly prepared on the substrate using the TAC method. The Cr/Au (5 nm/50 nm) electrode deposited on $PtSe_2$ film through magnetron sputtering technology was used as the top electrode, and the bottom electrode was formed by attaching an indium gallium (InGa) alloy to the back side of the n-Si substrate.

Material characterizations

The surface morphology of the $PtSe_2$ film was observed using a scanning electron microscope (SEM, Hitachi S-4800). The thickness and crystal structures of the $PtSe_2$ layers were characterized using an atomic force microscope (AFM, Bruker Dimension Edge) and X-ray diffraction (XRD, Bruker Dimension Edge). The thickness of the native ultrathin SiO_2 layer was estimated by using an ellipsometer (HORIBA UVISEL) and fitting with a classical model. The Raman spectra were measured on a Raman spectrometer (Renishaw inVia) using a 532-nm laser as the excitation light. The absorption spectra of the $PtSe_2$ layers grown on quartz substrates were measured by a UV-Vis-NIR spectrometer (Hitachi U-4100). The transmission electron microscopy (TEM) characterization was performed using a high-resolution TEM (HRTEM, JEM-2100F). Chemical structure analysis was conducted *via* X-ray photoelectron spectroscopy (XPS, Thermo ESCALAB 250Xi).

Device characterization

The photoelectric measurements of the devices were performed using a homemade system, including a semiconductor analyzer FS480 (PDA Co. Ltd), a pulse generator (RIGOL DG5100), an oscilloscope (WaveSurfer 3024, Teledyne), and a power meter (Newport 1931-C).

RESULTS AND DISCUSSION

Device structure and basic characterization

To construct the $PtSe_2$/ultrathin SiO_2/Si heterostructure PD (Fig. 1a), a $PtSe_2$ film with a thickness of approximately 12.42 nm was grown using the TAC method on the effective working area defined *via* conventional photolithography and the liftoff process (Fig. S1). First, the designed effective working area window (0.05 cm × 0.05 cm) was exposed and developed on the SiO_2/Si substrate covering the photoresist layer through a photolithography process. Then, the substrate was immersed in a BOE solution to completely remove the SiO_2 layer in the exposed window. Afterward, a suitable ultrathin SiO_2 layer (~3 nm, Fig. S2) was formed on the Si substrate in the working area. Subsequently, a Pt film was deposited in the effective working area and was converted into the 2D $PtSe_2$ film through the TAC method. Finally, the Cr/Au (5 nm/50 nm) electrode was deposited on the $PtSe_2$ film as the top electrode, and an InGa alloy was used as the bottom electrode to adhere to the back of the n-Si substrate.

We characterized the structure of the prepared $PtSe_2$ using various techniques. As shown in Fig. S3, the typical Raman spectrum of the $PtSe_2$ film excited by 532-nm light contains two prominent peaks at approximately 177.1 and 205.2 cm^{-1}, which are assigned to the E_{2g} in-plane vibration mode of Se atoms and A_{1g} out-of-plane vibration mode of Se atoms [22], respectively. Fig. 1b shows the optical image of the $PtSe_2$ film with a scratch and a picture of the $PtSe_2$ film on the SiO_2/Si substrate. The Raman mappings acquired from the marked square areas at 177.1 cm^{-1} (Fig. 1c) and 205.2 cm^{-1} (Fig. 1d) show a uniform intensity contrast, demonstrating the flatness and uniformity of the $PtSe_2$ film. To further confirm the uniformity of the $PtSe_2$ film, 16 test locations randomly distributed on the $PtSe_2$ film were analyzed by Raman spectroscopy (Fig. S4), which showed identical Raman characteristics. Together with the SEM image and 3D AFM topographical image (Fig. S5), these results suggest that the 2D $PtSe_2$ film with a root-mean-square roughness (R_q) of ~0.724 nm (Fig. S6) uniformly grew on the substrate. The thickness of the prepared $PtSe_2$ film is approximately 12.42 nm, as determined *via* the AFM profile analysis (Fig. S7). The XPS analysis (Fig. S8) was generally used to further detect the chemical composition of the $PtSe_2$ film and the binding energy of Se and Pt. Corrected with C 1s at 284.8 eV, the binding energies for the Pt $4f_{7/2}$ and Pt $4f_{5/2}$ are at 73.30 and 76.55 eV, and the binding energies for the Se $3d_{5/2}$ and Se $3d_{3/2}$ are located at 54.55 and 55.35 eV, respectively, which are in good agreement with the values in the literature [23]. The XRD patterns in Fig. S9 exhibit two diffraction peaks positioned at 16.74° and 32.92°, corresponding to the (001) and (101) crystal planes of $PtSe_2$, respectively. The full width at half maximum and grain size of the (001) peak are approximately 1.17° and 6.8 nm, which suggest a relatively good crystallinity. The HRTEM images (Fig. S10) show that the $PtSe_2$ film is a polycrystalline $PtSe_2$ layer with a vertically aligned layered structure. Fig. S10d reveals that a layer distance along (001) is approximately 0.54 nm. The diffraction rings from inside to outside can be readily ascribed to the (001), (100), (101), and (110) planes with a lattice spacing of 0.54, 0.32, 0.28, and 0.18 nm, respectively, from the selected-area electron diffraction pattern (Fig. S11). To confirm the existence of the SiO_2 layer underneath, we made a scratch on the $PtSe_2$ film sample and measured the area using energy-dispersive X-

© Science China Press and Springer-Verlag GmbH Germany, part of Springer Nature 2022

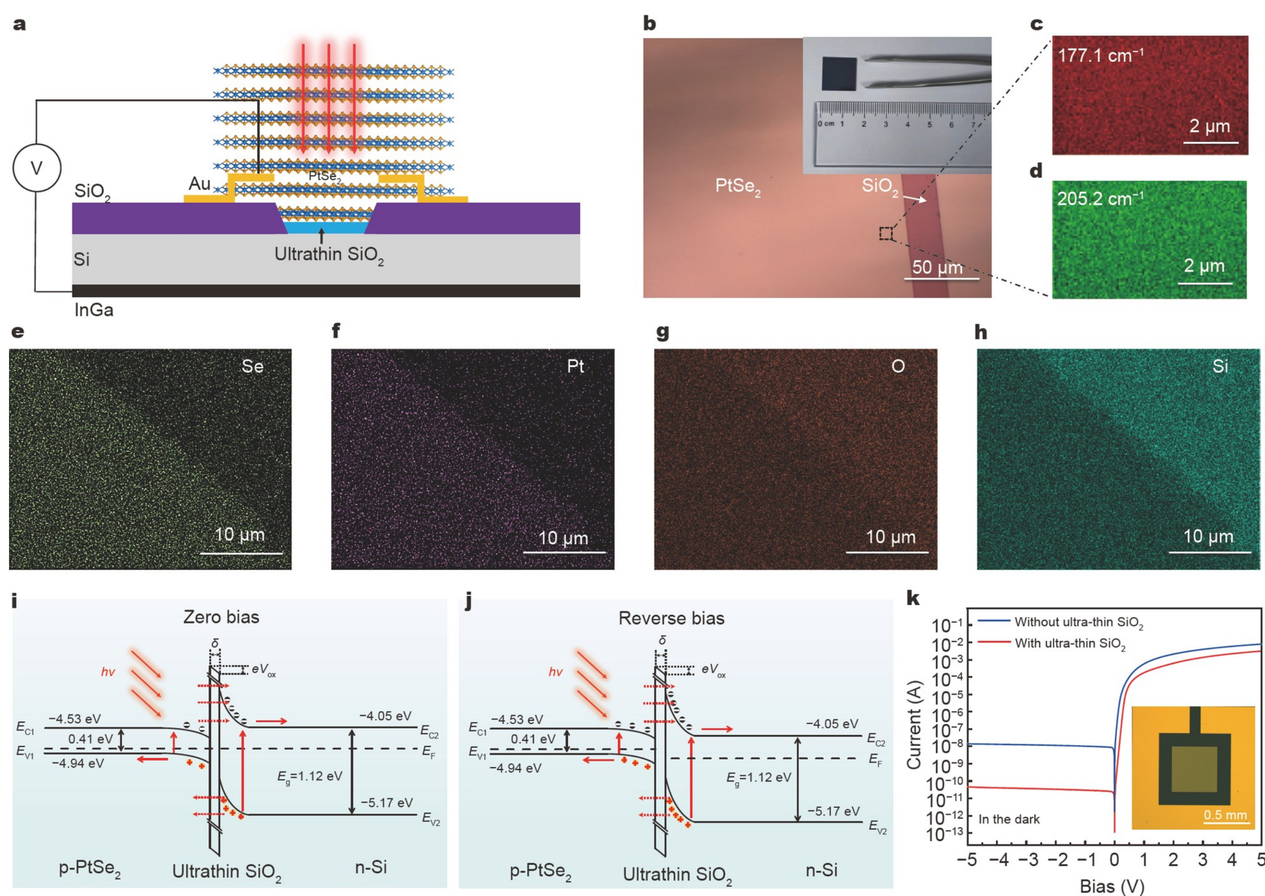

Figure 1 Device structure and basic characterization at room temperature. (a) Schematic diagram of the cross-sectional structure of the device. (b) Optical image of the $PtSe_2$ film with a scratch and inset showing a picture of the $PtSe_2$ film on the SiO_2/Si substrate. (c, d) Raman mappings acquired at 177.1 and 205.2 cm^{-1}. (e–h) Se, Pt, O, and Si elemental mappings of the prepared $PtSe_2$ sample on the substrate with the ultrathin SiO_2. (i, j) Energy-band diagrams of the $PtSe_2$/ultrathin SiO_2/Si heterojunction under zero bias and reverse bias under illumination. δ is the thickness of the oxide layer. V_{ox} is the potential drop across the oxide layer. The bandgap of the silicon is approximately 1.12 eV. The bandgap of our $PtSe_2$ is approximately 0.41 eV. (k) *I-V* curves of PDs with and without ultrathin SiO_2 in the dark; the inset shows an optical image of an as-fabricated PD.

ray spectroscopy to obtain elemental mappings (Fig. 1e–h). The Se and Pt elements are evenly distributed in the lower left area, and the O and Si signals are clearly observed in the measured upper right area. The existence of an ultrathin SiO_2 on Si was further confirmed *via* ellipsometry (Fig. S2).

Fig. 1i, j show the band diagrams of the heterojunction under zero bias and reverse bias. As shown by the Tauc plot (Fig. S12) and UV photoelectron spectroscopy measurement (Fig. S13), the Fermi level (E_F) of the multilayered $PtSe_2$ is located at ~4.84 eV. In a rough estimation, the work function of n-Si with a resistivity of 1–10 Ω cm is ~4.25 eV. When the two components are in close contact with each other in the dark, electrons diffuse from the n-Si to p-$PtSe_2$ as confirmed by the Hall effect measurement (Table S1) to achieve a thermal equilibrium due to the difference in the work functions of the n-Si (~4.25 eV) and p-$PtSe_2$ film (~4.84 eV). Meanwhile, the positively charged empty states are thus left inside the Si to form a depletion region. This charge transfer process will continue until the E_F is aligned in the heterostructure. As a result, the energy levels near the n-Si surface bend upwards, and a strong built-in electric field is formed at the interface of the p-n heterostructure. Under the irradiation of light, electron-hole pairs are generated within and near the depletion region, which can be quickly and effectively separated by the existing built-in electric field to form a considerable photocurrent. In the case of the reverse bias, the depletion region can be effectively expanded to allow more photocarriers to participate in the generation of photocurrents. Therefore, a reverse bias external electric field can effectively improve the separation efficiency of photogenerated electron-hole pairs. However, limited by the number of electron-hole pairs generated, the current will approach saturation under a certain negative bias.

Compared with the $PtSe_2$/Si heterojunction structure, the performance of the PD based on the $PtSe_2$/ultrathin SiO_2/Si heterojunction is much more excellent. Due to the tunneling effect [4,24,25], the ultrathin SiO_2 layer has little effect on the carrier transport under a bias. The dielectric ultrathin SiO_2 layer separates the $PtSe_2$ from the Si, thereby increasing the interfacial potential barrier height. This action can effectively suppress the dark current of the PD and greatly improve the performance of the device. Furthermore, the bonding feature of the ultrathin SiO_2 naturally grown at the Si surface passivates the Si surface by reducing dangling bonds and defect states and thus can greatly reduce carrier recombination at the interface, which is also beneficial to suppressing the dark current [26,27].

We elucidate the influence of the ultrathin interface oxide layer on the $PtSe_2$/Si heterojunction as follows. The current-voltage relationship of the $PtSe_2$/Si can be described by the

 © Science China Press and Springer-Verlag GmbH Germany, part of Springer Nature 2022

thermionic emission theory [21]:

$$I = I_s\left[\exp\left(\frac{qV}{nkT}\right) - 1\right], \quad (1)$$

$$I_s = AA^*T^2\exp\left(-\frac{\Phi_B}{kT}\right), \quad (2)$$

where I_s is the reverse saturation current, n is the ideality factor, A is the effective working area of the PD, A^* is the effective Richardson constant, T is the absolute temperature, q is the electronic charge, Φ_B is the interfacial potential barrier height of the p-n junction, and k is the Boltzmann constant. After inserting an ultrathin SiO_2 layer in the interface of the $PtSe_2$/Si heterojunction, the reverse saturation current of the $PtSe_2$/ultrathin SiO_2/Si heterojunction can be modified as [28]

$$I_s = AA^*T\exp\left(-\sqrt{\chi_{ox}}\delta\right)\exp\left(-\frac{\Phi_B}{kT}\right), \quad (3)$$

where χ_{ox} and δ are the mean barrier height and thickness of the SiO_2 layer, respectively. The term $\exp\left(-\sqrt{\chi_{ox}}\delta\right)$ is the transmission coefficient across the thin interfacial SiO_2 layer. According to Equation (3), the existence of a SiO_2 layer can effectively suppress the reverse saturation current. However, as the thickness of the SiO_2 layer increases, the transmission coefficient rapidly decreases. As a result, the carriers will not pass through the interfacial oxide layer efficiently. Therefore, I_{dark} of our $PtSe_2$/ultrathin SiO_2/Si heterojunction PD is much lower than that of the traditional $PtSe_2$/Si heterojunction PD regardless of whether it is at zero bias or negative bias.

Fig. 1k plots the current-voltage (*I-V*) curves on a semilogarithmic scale for PDs with and without ultrathin SiO_2 in the dark. Striking current rectifying characteristics are observed. The rectification ratio of the PD with an ultrathin SiO_2 (5.7×10^7 within ±5 V) is a two-order magnitude higher than that of the PD without an ultrathin SiO_2 (5.5×10^5 within ±5 V). Considering the ohmic contact of the Au/$PtSe_2$ and InGa/Si contacts (Fig. S14), this rectification characteristic is completely derived from the $PtSe_2$/ultrathin SiO_2/Si heterojunction. Particularly, the diode ideality factor (n) calculated from the ln*I-V* curve is 1.015 in the dark (Fig. S15a), which is superior to that of previous reports [20,21,23]. This value is perfectly close to that of an ideal diode (n = 1), indicating that the interface recombination is very low in the $PtSe_2$/ultrathin SiO_2/Si heterostructure. As clearly shown in Fig. S16, I_{dark} of the $PtSe_2$/ultrathin SiO_2/Si heterojunction PD is 0.12 pA and 0.03 nA at 0 and −1 V, respectively, whereas I_{dark} of the $PtSe_2$/Si heterojunction PD is 3.2 pA and 11.2 nA at 0 and −1 V, respectively. The dark current of the $PtSe_2$/ultrathin SiO_2/Si is also much smaller than those of the previously reported $PtSe_2/AlO_x$/Si (0.8 pA) and $PtTe_2$/Si (~10 pA) PDs. Moreover, the built-in potential barrier (V_{bi}) of the $PtSe_2$/ultrathin SiO_2/Si heterojunction was calculated as 1.04 V, which is more than double that (0.46 eV) of the $PtSe_2$/Si heterojunction (Fig. S17). Hence, the $PtSe_2$/ultrathin SiO_2/Si heterojunction PD can separate carriers more efficiently and generate a larger photoresponse current. The above results suggest that the $PtSe_2$/ultrathin SiO_2/Si heterojunction with a better diode quality has been achieved.

Photoresponse properties

We performed a series of photoelectric performance characterizations of the fabricated device. The *I-V* curves of the $PtSe_2$/ultrathin SiO_2/Si PD exposed to different light power densities (0.0000097–101.57 mW cm^{-2}) under 808-nm illumination show a significant light response (Fig. 2a). As shown in Fig. S18, the

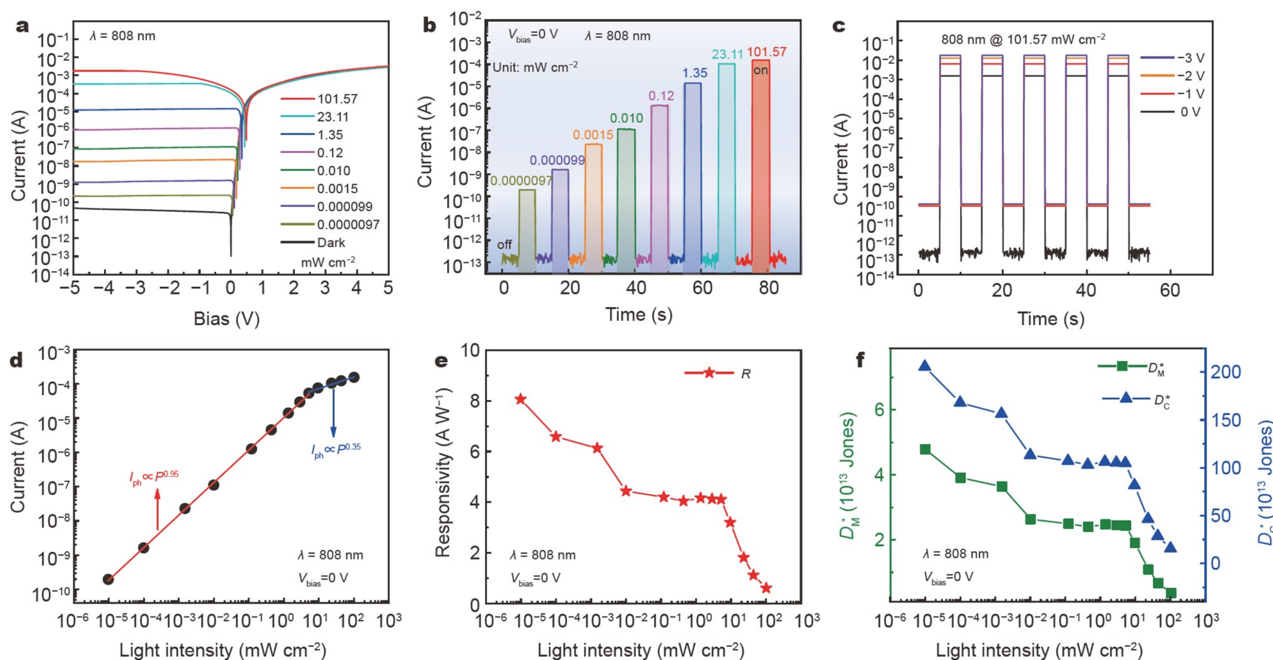

Figure 2 Optoelectronic characteristics of the $PtSe_2$/ultrathin SiO_2/Si heterojunction PD under 808-nm laser illumination at room temperature. (a) *I-V* curves of the device under 808-nm laser illumination with increasing light intensities. (b) Time-dependent photoresponse of the PD under 808-nm illumination at zero bias. (c) Time-dependent photoresponse of the PD under different biases. (d) Photocurrent at different incident intensities under zero bias and the fitting relationship between the photocurrent and light intensity. (e) Responsivity as a function of light intensity. (f) Specific detectivity, D_M^* and D_C^*, as a function of light intensity. The calculation of D_M^* is based on the consideration of noise. To facilitate the comparison with the previous devices, D_C^* is calculated under the condition of underestimating the noise.

© Science China Press and Springer-Verlag GmbH Germany, part of Springer Nature 2022

PD achieves a high photoelectric conversion efficiency (PEC) of ~19% under 808-nm illumination (23.11 mW cm^{-2}), which is higher than the traditional $PtSe_2$/Si (~8%) [20]. In this case, the photovoltage and photocurrent are 0.435 V and 0.104 mA, respectively. In addition, the device can earn a good PEC of ~5.4% under standard illumination (AM1.5, 100 mW cm^{-2}). This behavior with light response at zero bias allows our heterojunction to be used as a self-driven PD operating without an external power supply [29,30]. The time-dependent photoresponse under periodic switching of the 808-nm NIR illumination at zero bias (Fig. 2b) suggests that the device is extremely sensitive to the incident light, enabling a stable and reversible switching between high-conductance (e.g., ~155 μA at 101.57 mW cm^{-2}) and low-conductance (e.g., ~0.12 pA in the dark) states, which offers a prominent I_{light}/I_{dark} ratio of 1.29×10^9 at zero bias under 808-nm illumination with 101.57 mW cm^{-2}. The performance of our $PtSe_2$/ultrathin SiO_2/Si heterojunction PD is superior to that of other reported heterostructure PDs based on 2D materials (Tables S2 and S3). Furthermore, our heterojunction PD has a high I_{light}/I_{dark} ratio of 1.63×10^3 even at a low optical power density of 0.0097 μW cm^{-2}, indicating that the PD can be used to detect weak light signals.

By further studying the photoresponse characteristics under different voltages (Fig. 2c), we find that the switching ratio can be manipulated by the reverse bias under the irradiation (808 nm, 101.57 mW cm^{-2}). The dark current from 0 to −3 V increases more significantly than the photocurrent, resulting in a decrease in the I_{light}/I_{dark} ratio from 1.29×10^9 to 4.27×10^7. The reverse bias can effectively extend the depletion region and improve the separation efficiency of photogenerated electron-hole pairs, thus allowing more electron-hole pairs to join the generation of the response current. As a result, the responsivity values from 0 to −3 V are increased from 0.61 to 6.9 A W^{-1}. By contrast, the photocurrent from −3 to −5 V negligibly increases (Fig. 2a) due to the limited extra number of photogenerated carriers and the nonnegligible recombination loss.

Fig. 2d and Fig. S19 reveal the fact that the photocurrent and photovoltage of the PD are highly dependent on the power density and increase with the increase in the light intensity, which is explained by the increased number of photocarriers at a higher light intensity. The photovoltage can reach 0.486 V under the irradiation of 101.57 mW cm^{-2}. However, with further increase in light intensity, the photovoltage increases slowly (Fig. S19). Moreover, there is a similar trend between photocurrent and power density. To understand the underlying reasons for this phenomenon, the relationship between photocurrent and light power density can be explained by the following formula [31].

$$I_{ph}=aP^{\theta}, \quad (4)$$

where I_{ph} is the difference between I_{light} and I_{dark}, a is a constant for a known wavelength, P is the light power density, and exponent θ is an empirical value reflecting the recombination of optically excited carriers. By fitting the data, a nearly ideal value of $\theta = 0.95$ (Fig. 2d) is obtained in the light power density range (0.0000097–9.47 mW cm^{-2}), indicating that the recombination loss can be ignored in this range. Meanwhile, an undesirable value of $\theta = 0.35$ is obtained in a higher power density range (9.47–101.57 mW cm^{-2}), implying that the recombination loss turns prominent in this range [32]. Such an experimental phenomenon is caused by the nonnegligible recombination loss of carriers because of the growing concentration of photogenerated carriers in the $PtSe_2$/ultrathin SiO_2/Si heterojunction.

Generally, the linear dynamic range (LDR) is an important performance parameter used to characterize PDs, usually expressed as follows [33]:

$$\mathrm{LDR} = 20\log\left(\frac{I^{*}_{ph}}{I_{dark}}\right), \quad (5)$$

where I^{*}_{ph} is the photocurrent measured at a light power density of 1 mW cm^{-2} (here, the corresponding current is ~9.97 μA) and I_{dark} of ~0.12 pA. The LDR of the PD is 158.4 dB, which exceeds that (120 dB) of a traditional silicon photodiode [33]. The large LDR value proves that the recombination loss of the device in a certain light power density region is quite low, which is fully consistent with the results above.

To further evaluate the performance of our PD based on the $PtSe_2$/ultrathin SiO_2/Si heterojunction, the responsivity (R) was accurately calculated. Generally, R is described as the ratio of the output current of photoresponse to the incident light power current in the effective working area of the PD. The parameter is usually obtained from the experimental data using the formula [34]:

$$R = \frac{I_{light} - I_{dark}}{P_{in}} = \mathrm{EQE}\left(\frac{q\lambda}{hc}\right), \quad (6)$$

where P_{in}, represents the input optical power ($P_{in} = PA$; P is the optical power density and A is the effective device area), EQE represents external quantum efficiency, q, λ, h, and c represent the elementary charge, wavelength of the incident light, Planck's constant, and speed of light, respectively. According to our experimental data, R at room temperature is obtained in Fig. 2e under different light power densities under illumination with 808-nm laser at zero bias. R of the $PtSe_2$/ultrathin SiO_2/Si heterojunction reaches the highest value of 8.06 A W^{-1} under a light intensity of 0.0099 μW cm^{-2} at the zero bias voltage, which is far higher than that of the previously reported self-driven PDs (Tables S2 and S3) and commercial Si P-I-N PDs (less than 0.5 A W^{-1}).

Furthermore, we consider the specific detectivity (D^*) and noise equivalent power (NEP), which reflects the detection ability of a PD to weak light signals from noise. To calculate D^*, the noise density spectrum (Fig. S20) was measured. The noise spectral density shows a strong 1/f component, indicating that flicker (1/f) noise dominates the noise current in the PD. The noise current density i_N is extracted as 8.42×10^{-15} A Hz$^{-1/2}$ at a frequency of Δf = 10 kHz. Here, D^* is denoted as D_M^*, calculated by the following formula [35,36]:

$$D_M^* = \frac{(AB)^{1/2}}{\mathrm{NEP}}, \quad (7)$$

$$\mathrm{NEP} = \frac{i_N}{R}, \quad (8)$$

where A (0.0025 cm^2) and i_N (8.42×10^{-15} A Hz$^{-1/2}$) are the effective device area and noise current density (Fig. S7) at a frequency of Δf = 10 kHz, respectively. B is the bandwidth. Thus, D_M^* of our $PtSe_2$/ultrathin SiO_2/Si heterojunction PD is 4.78×10^{13} Jones at 808-nm NIR light irradiation with a light power density of 0.0099 μW cm^{-2} at zero bias (Fig. 2f, left y-axis), and the NEP is 1.04×10^{-15} W Hz$^{1/2}$. D_M^* of our detector is much better than the best available value of previously reported Si-

© Science China Press and Springer-Verlag GmbH Germany, part of Springer Nature 2022

based PDs with 2D TMDs (Table S2) [37–39]. In addition, for many previous studies on 2D material-based PDs, D^* is generally estimated based on the direct current dark noise when the noise is dominated by the $1/f$ noise [40]. To facilitate the comparison with the performance of previous studies, we also used this method to estimate D^* (see Supplementary information). The calculated results (here, D^* is denoted as D_C^*) are also shown in Fig. 2f (right y-axis). Surprisingly, the estimated D_C^* is nearly two orders of magnitude larger than D_M^* due to the underestimated noise current. In addition, R and D_M^* decreased with the increase in the light power density (Fig. 2e, f), which is consistent with previous reports [21,22].

The response speed is also one of the most important parameters of the PD, which reflects the ability of the PD to rapidly track changing light signals. We recorded the output photocurrent changes with time under different frequencies (1–100 kHz; Fig. S21) of optical signal provided by an 808-nm laser diode driven by a function generator. The relative balance $(I_{max} - I_{min})/I_{max}$ of the photocurrent as a function of frequency declined very slowly, and it maintained approximately 70.5% of its maximum value at a frequency of 30 kHz. Moreover, the 3 dB frequency is defined as the frequency at which the light response drops to the maximum light response value of 70.7% [41]. Therefore, the 3 dB frequency was calculated as ~30 kHz, which indicates that the device can exhibit a fast response speed, good repeatability, and excellent switching characteristics below the frequency of 30 kHz. In the time domain, the response speed is defined as the total time required for the output to rise from 10% of the pulse peak value to 90% and fall from 90% to 10%. The estimated rise time τ_r and fall time τ_f under a pulsed 808-nm NIR illumination at a frequency of 20 kHz are 14.1 and 15.4 μs, respectively (Fig. S21). This relatively fast response speed is related to the special device structure, which is conducive to the rapid separation and transport of light-excited carriers. The above results indicate that our $PtSe_2$/ultrathin SiO_2/Si heterojunction PD can monitor fast optical signals, promising for high-speed optical detection. However, the intrinsic carrier dynamic speed of $PtSe_2$ is in the order of picosecond (~3 ps) as measured by the optical pump-probe experiment (Fig. S22) and previous work [42]. This finding indicates that $PtSe_2$ can be used to fabricate high-speed PDs by optimizing device architectures [43]. Moreover, a clean heterojunction interface is beneficial for reducing the number of interface defects, thereby reducing the probability of photogenerated carrier trapping/de-trapping while supporting a fast response speed.

We evaluated the broad-spectrum and sensitive photoresponse performance of our $PtSe_2$/ultrathin SiO_2/Si PD. As shown in Fig. 3a, b, strong photoresponse characteristics are

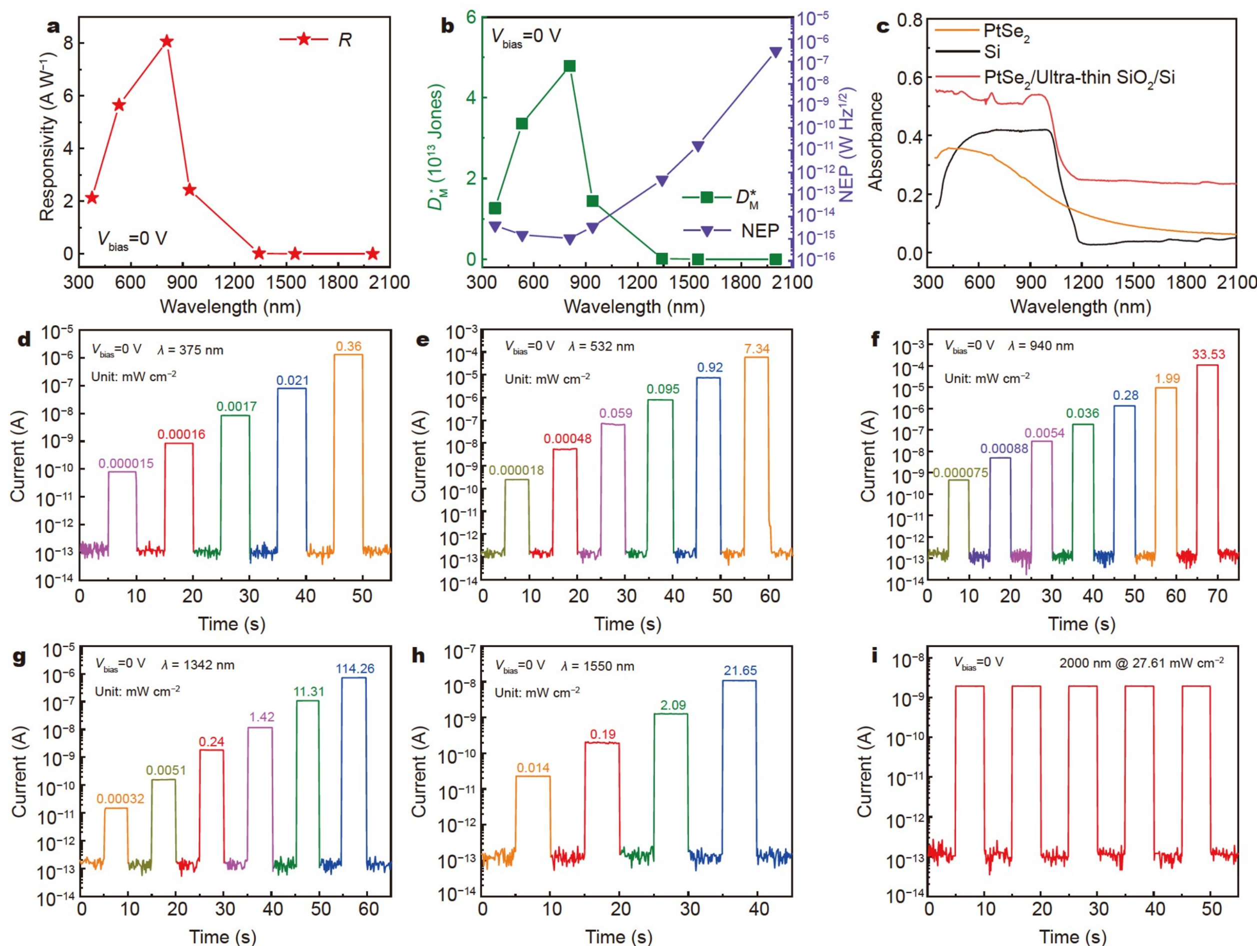

Figure 3 Optoelectronic characteristics of the $PtSe_2$/ultrathin SiO_2/Si heterojunction PD under different wavelength light illuminations at zero bias and room temperature. (a) Responsivity as a function of incident light wavelength. (b) Specific detectivity and NEP as a function of incident light wavelength. (c) UV-Vis-NIR absorption spectra of the $PtSe_2$, n-Si, and $PtSe_2$/ultrathin SiO_2/Si heterojunctions. (d–i) Photoresponse of the PD under 375, 532, 940, 1342, 1550, and 2000 nm light illuminations at zero bias.

 © Science China Press and Springer-Verlag GmbH Germany, part of Springer Nature 2022

observed over a wide wavelength spectrum as measured from 375 to 2000 nm, demonstrating the broadband detection capability of the $PtSe_2$/ultrathin SiO_2/Si PD. The large *R* in the UV-Vis-NIR spectral region (375–940 nm) indicates that incident photons can be converted into charge carriers very efficiently. Furthermore, benefiting from the pronounced NIR optical absorption of the multilayered $PtSe_2$ (Fig. 3c), the PD exhibits reliable light response characteristics under NIR radiation at the wavelengths of 1342 nm (Fig. 3g), 1550 nm (Fig. 3h), and 2000 nm (Fig. 3i). This outcome shows its potential in the NIR field. Compared with the traditional $PtSe_2$/Si PD (Fig. S23), the $PtSe_2$/ultrathin SiO_2/Si PD exhibits a better response current under the measured wavelengths.

Integration of devices

To demonstrate the potential of the $PtSe_2$/ultrathin SiO_2/Si heterojunction PD for device integration and the uniformity of the photoelectric response of a large number of the devices, we fabricated a 9 × 9 device array (Fig. 4a). Fig. 4b shows the dark current and photocurrent of these devices in the array under 808-nm illumination with 13.36 mW cm^{-2} at zero bias. The dark currents of the 81 devices range from 0.07 to 0.18 pA, with an average value of 0.12 pA. The photocurrents of the 81 devices range from 80.7 to 98.7 μA, with an average value of 91.0 μA. As plotted in Fig. 4c, the rectification ratio of all the 81 devices within ±5 V (Fig. S24) is in the range from 4.92×10^7 to 6.48×10^7, with an average value of 5.7×10^7. Such minor fluctuations of the dark current, photocurrent, and rectification ratios suggest a very good uniformity of our devices.

We further studied the ability of the PD array to record images under different wavelengths of light. Fig. 4d–f are the schematic diagrams for testing the response of the devices under UV (375 nm, 0.12 mW cm^{-2}), Vis (532 nm, 0.51 mW cm^{-2}), and NIR (1550 nm, 7.42 mW cm^{-2}) lights, respectively. After placing the corresponding self-made masks, homogeneous light irradiation was projected onto the PD array. Hence, only the devices in the hollow areas that were not shaded could be illuminated, whereas the other devices were kept in the dark. Then, the currents of all the devices were measured independently, and the results were described by a 9 × 9 2D contrast current map. As

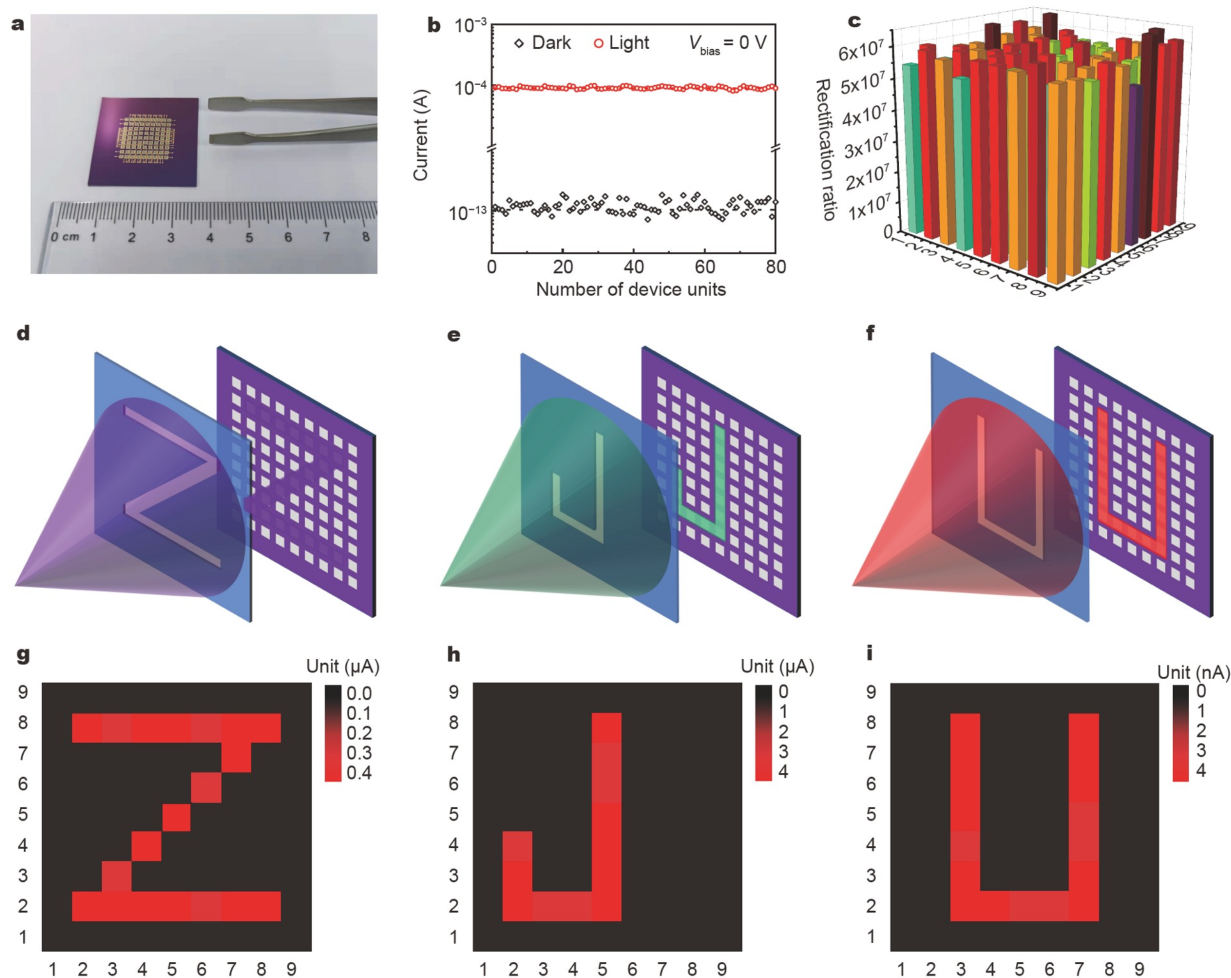

Figure 4 Optoelectronic characteristics of the 9 × 9 device array based on the $PtSe_2$/ultrathin SiO_2/Si heterojunction PD under different wavelength light illuminations at room temperature. (a) Optical image of the prepared 9 × 9 device array based on the $PtSe_2$/ultrathin SiO_2/Si heterojunction PD. (b) Currents in darkness and under 808-nm illumination for the 9 × 9 devices in the array. The dashed lines denote the average values for the dark current (black) and photocurrent (red). (c) 3D diagram of the rectification ratio for each device in the array within ±5 V. (d–f) Schematic illustration of the setup for UV, Vis, and NIR light imaging. (g–i) 2D current contrast map of the PD array corresponding to UV (375 nm, 0.12 mW cm^{-2}), Vis (532 nm, 0.51 mW cm^{-2}), and NIR (1550 nm, 7.42 mW cm^{-2}) light irradiations, demonstrating the ability to record the images of "Z," "J", and "U" letters under UV-Vis-NIR illumination.

© Science China Press and Springer-Verlag GmbH Germany, part of Springer Nature 2022

shown in Fig. 4g–i, the shapes of the "Z," "J", and "U" letters can be easily and accurately recognized with a reasonable spatial resolution, showing the potential for UV-Vis-NIR light image sensing. Furthermore, the array density can be increased by further reducing the area of an individual device to increase the spatial resolution.

In practical applications, the long-term stability of the PD in an ambient environment is a crucial parameter. We investigated the ambient stability of our $PtSe_2$/ultrathin SiO_2/Si heterojunction PD stored in an ambient environment for seven months without packaging. Negligible degradation was observed in terms of rectification, photovoltaic behavior, response speed, and time-varying light response (Fig. S25), verifying its superior ambient stability. Such excellent stability is attributed not only to the outstanding characteristics of $PtSe_2$, such as air stability and dense morphology, but also to the natively grown ultrathin SiO_2 layer, which prevents gas penetration into the interfaces of the device.

CONCLUSIONS

In this paper, we report a room-temperature high-performance, air-stable, self-driven, and broadband PD based on the $PtSe_2$/ultrathin SiO_2/Si heterojunction. Compared with other relevant detectors, our PD with ultrathin SiO_2 exhibits significant advantages of promising broadband responsivity, high specific detectivity, rapid response speed, and extremely low dark current. The PD shows an extremely low I_{dark} of approximately 0.12 pA with a diode ideality factor (n) of 1.015 and a high rectification ratio of 5.7×10^7 in the dark. Under 808-nm illumination at zero bias, the device shows outstanding photoresponse characteristics in terms of a large I_{light}/I_{dark} ratio of 1.29×10^9, an excellent responsivity of 8.06 A W^{-1}, a specific detectivity of 4.78×10^{13} Jones, and a rapid response speed of 14.1/15.4 μs. In addition, the photocurrent responsivities of the PD illuminated under 375, 532, and 940 nm are 2.12, 5.56, and 2.43 A W^{-1}, respectively. Benefiting from the strong NIR absorption of $PtSe_2$ films, the PD also has great photocurrent responsivities at the wavelengths of 1342 and 1550 nm, which are 18.12 and 0.65 mA W^{-1}, respectively. Moreover, the facile fabrication of our PD renders it inherently easy to integrate with Si-based CMOS technologies. The incorporation of an ultrathin insulating layer into the heterostructure interface of devices can block the dark current without suppressing the photocurrent to achieve an astonishing performance, proving a general strategy to improve the performance of PDs and energy conversion cells.

Received 4 March 2022; accepted 16 May 2022; published online 21 July 2022

1 Dhyani V, Das S. High-speed scalable silicon-MoS_2 p-n heterojunction photodetectors. Sci Rep, 2017, 7: 1–9
2 Xu Z, Lin S, Li X, *et al.* Monolayer MoS_2/GaAs heterostructure self-driven photodetector with extremely high detectivity. Nano Energy, 2016, 23: 89–96
3 Qiao H, Huang Z, Ren X, *et al.* Self-powered photodetectors based on 2D materials. Adv Opt Mater, 2020, 8: 1900765
4 Zeng L, Wu D, Jie J, *et al.* Van der Waals epitaxial growth of mosaic-like 2D platinum ditelluride layers for room-temperature mid-infrared photodetection up to 10.6 μm. Adv Mater, 2020, 32: 2004412
5 Li X, Zhu M, Du M, *et al.* High detectivity graphene-silicon heterojunction photodetector. Small, 2016, 12: 595–601
6 Rogalski A. HgCdTe infrared detector material: History, status and outlook. Rep Prog Phys, 2005, 68: 2267–2336
7 Kimukin I, Biyikli N, Kartaloglu T, *et al.* High-speed InSb photodetectors on GaAs for mid-IR applications. IEEE J Sel Top Quantum Electron, 2004, 10: 766–770
8 Long M, Wang P, Fang H, *et al.* Progress, challenges, and opportunities for 2D material based photodetectors. Adv Funct Mater, 2019, 29: 1803807
9 Bhimanapati GR, Lin Z, Meunier V, *et al.* Recent advances in two-dimensional materials beyond graphene. ACS Nano, 2015, 9: 11509–11539
10 Tan C, Zhang H. Two-dimensional transition metal dichalcogenide nanosheet-based composites. Chem Soc Rev, 2015, 44: 2713–2731
11 Chhowalla M, Shin HS, Eda G, *et al.* The chemistry of two-dimensional layered transition metal dichalcogenide nanosheets. Nat Chem, 2013, 5: 263–275
12 Xu M, Liang T, Shi M, *et al.* Graphene-like two-dimensional materials. Chem Rev, 2013, 113: 3766–3798
13 Akinwande D, Huyghebaert C, Wang CH, *et al.* Graphene and two-dimensional materials for silicon technology. Nature, 2019, 573: 507–518
14 Cao B, Ye Z, Yang L, *et al.* Recent progress in van der Waals 2D $PtSe_2$. Nanotechnology, 2021, 32: 412001
15 Gong Y, Lin Z, Chen YX, *et al.* Two-dimensional platinum diselenide: Synthesis, emerging applications, and future challenges. Nano-Micro Lett, 2020, 12: 1–34
16 Wang Y, Li L, Yao W, *et al.* Monolayer $PtSe_2$, a new semiconducting transition-metal-dichalcogenide, epitaxially grown by direct selenization of Pt. Nano Lett, 2015, 15: 4013–4018
17 Yu X, Yu P, Wu D, *et al.* Atomically thin noble metal dichalcogenide: A broadband mid-infrared semiconductor. Nat Commun, 2018, 9: 1545
18 Zeng LH, Lin SH, Li ZJ, *et al.* Fast, self-driven, air-stable, and broadband photodetector based on vertically aligned $PtSe_2$/GaAs heterojunction. Adv Funct Mater, 2018, 28: 1705970
19 Wu D, Wang Y, Zeng L, *et al.* Design of 2D layered $PtSe_2$ heterojunction for the high-performance, room-temperature, broadband, infrared photodetector. ACS Photonics, 2018, 5: 3820–3827
20 Xie C, Zeng L, Zhang Z, *et al.* High-performance broadband heterojunction photodetectors based on multilayered $PtSe_2$ directly grown on a Si substrate. Nanoscale, 2018, 10: 15285–15293
21 Ma M, Chen H, Zhou K, *et al.* Multilayered $PtSe_2$/pyramid-Si heterostructure array with light confinement effect for high-performance photodetection, image sensing and light trajectory tracking applications. J Mater Chem C, 2021, 9: 2823–2832
22 Zeng L, Lin S, Lou Z, *et al.* Ultrafast and sensitive photodetector based on a $PtSe_2$/silicon nanowire array heterojunction with a multiband spectral response from 200 to 1550 nm. NPG Asia Mater, 2018, 10: 352–362
23 Zhuo R, Zeng L, Yuan H, *et al.* *In-situ* fabrication of $PtSe_2$/GaN heterojunction for self-powered deep ultraviolet photodetector with ultrahigh current on/off ratio and detectivity. Nano Res, 2019, 12: 183–189
24 Ng KK, Card HC. A comparison of majority- and minority-carrier silicon MIS solar cells. IEEE Trans Electron Devices, 1980, 27: 716–724
25 Zhang H, Zhang X, Liu C, *et al.* High-responsivity, high-detectivity, ultrafast topological insulator Bi_2Se_3/silicon heterostructure broadband photodetectors. ACS Nano, 2016, 10: 5113–5122
26 He L, Jiang C, Wang H, *et al.* High efficiency planar Si/organic heterojunction hybrid solar cells. Appl Phys Lett, 2012, 100: 073503
27 Aberle AG. Surface passivation of crystalline silicon solar cells: A review. Prog Photovolt-Res Appl, 2000, 8: 473–487
28 Card HC, Rhoderick EH. Studies of tunnel MOS diodes I. Interface effects in silicon Schottky diodes. J Phys D-Appl Phys, 1971, 4: 1589–1601
29 Buscema M, Groenendijk DJ, Steele GA, *et al.* Photovoltaic effect in few-layer black phosphorus PN junctions defined by local electrostatic gating. Nat Commun, 2014, 5: 1–6
30 Lv Q, Yan F, Wei X, *et al.* High-performance, self-driven photodetector based on graphene sandwiched GaSe/WS_2 heterojunction. Adv Opt Mater, 2018, 6: 1700490
31 Wang L, Jie J, Shao Z, *et al.* MoS_2/Si heterojunction with vertically

 © Science China Press and Springer-Verlag GmbH Germany, part of Springer Nature 2022

standing layered structure for ultrafast, high-detectivity, self-driven visible-near infrared photodetectors. Adv Funct Mater, 2015, 25: 2910–2919
32 Xie C, Yan F. Flexible photodetectors based on novel functional materials. Small, 2017, 13: 1701822
33 Gong X, Tong M, Xia Y, *et al.* High-detectivity polymer photodetectors with spectral response from 300 nm to 1450 nm. Science, 2009, 325: 1665–1667
34 Choi W, Cho MY, Konar A, *et al.* High-detectivity multilayer MoS_2 phototransistors with spectral response from ultraviolet to infrared. Adv Mater, 2012, 24: 5832–5836
35 Tong L, Peng M, Wu P, *et al.* Hole-dominated Fowler-Nordheim tunneling in 2D heterojunctions for infrared imaging. Sci Bull, 2021, 66: 139–146
36 Fang Y, Armin A, Meredith P, *et al.* Accurate characterization of next-generation thin-film photodetectors. Nat Photon, 2018, 13: 1–4
37 Yang S, Pi L, Li L, *et al.* 2D $Cu_9S_5/PtS_2/WSe_2$ double heterojunction bipolar transistor with high current gain. Adv Mater, 2021, 33: 2106537
38 Wang F, Luo P, Zhang Y, *et al.* Band structure engineered tunneling heterostructures for high-performance visible and near-infrared photodetection. Sci China Mater, 2020, 63: 1537–1547
39 Lv L, Zhuge F, Xie F, *et al.* Reconfigurable two-dimensional optoelectronic devices enabled by local ferroelectric polarization. Nat Commun, 2019, 10: 3331
40 Choi MS, Qu D, Lee D, *et al.* Lateral MoS_2 p-n junction formed by chemical doping for use in high-performance optoelectronics. ACS Nano, 2014, 8: 9332–9340
41 Wu E, Wu D, Jia C, *et al.* *In situ* fabrication of 2D WS_2/Si type-II heterojunction for self-powered broadband photodetector with response up to mid-infrared. ACS Photonics, 2019, 6: 565–572
42 Wang G, Wang K, McEvoy N, *et al.* Ultrafast carrier dynamics and bandgap renormalization in layered $PtSe_2$. Small, 2019, 15: 1902728
43 Wang Y, Yu Z, Tong Y, *et al.* High-speed infrared two-dimensional platinum diselenide photodetectors. Appl Phys Lett, 2020, 116: 211101

Acknowledgements This work was supported by the National Natural Science Foundation of China (62090030/62090031, 51872257, and 51672244), the National Key R&D Program of China (2021YFA1200502), and the Natural Science Foundation of Zhejiang Province, China (LZ20F040001). The authors thank Dr. Yanjun Fang and Dr. Haiming Zhu for discussion.

Author contributions Ye P and Xu M conceived the idea and designed the experiments. Ye P performed the experiments with the assistance of Xiao H, Zhu Q, Kong Y, and Tang Y. Ye P and Xu M analyzed the data. Ye P and Xu M co-wrote the manuscript. All authors discussed the results.

Conflict of interest The authors declare that they have no conflict of interest.

Supplementary information Supporting data are available in the online version of the paper.

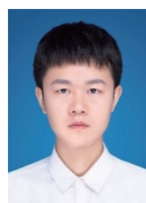

Peng Ye received his BSc degree from Huazhong University of Science and Technology, China. He is currently a graduate student at the College of Information Science and Electronic Engineering, Zhejiang University, China. His main research interest focuses on photodetectors and photoelectronic devices based on 2D materials.

Mingsheng Xu is a full professor at the School of Micro-Nano Electronics/College of Information Science and Electronic Engineering, Zhejiang University. He earned his PhD degree from the Department of Electronic Engineering, The Chinese University of Hong Kong. His current main research includes 2D materials and devices.

与硅基CMOS兼容且具有超高响应率和比探测率的二维二硒化铂自驱动光电探测器

叶鹏, 肖涵, 朱清海, 孔宇晗, 唐幼梅, 徐明生*

摘要 因二维材料的独特性质及其可调谐的光谱响应, 基于二维材料的光电探测器受到广泛关注. 然而, 它们的性能还不够突出, 其制造工艺与硅基互补金属氧化物半导体技术工艺流程的兼容性还需要评估. 在本文中, 我们报道了一种基于二硒化铂/超薄二氧化硅/硅异质结构的高性能、空气稳定、自驱动、室温宽带光电探测器. 该光电探测器表现出超高的响应度(8.06 A W^{-1})和比探测率(4.78 × 10^{13} cm $Hz^{1/2}$ W^{-1})、极低的暗电流(0.12 pA)以及优秀的开关比(1.29 × 10^9). 在375, 532, 1342和1550 nm波长处所测的光电流响应度分别为2.12, 5.56, 18.12和0.65 mA W^{-1}. 此外, 制造的9 × 9器件阵列不仅展示了该探测器非常好的均匀性和可重复性, 而且还显示了其在紫外-可见-近红外照明成像应用领域的潜力. 我们设计的二硒化铂/超薄二氧化硅/硅异质结光电探测器极大地抑制了暗电流, 提高了二极管的理想因子并增加了界面势垒. 因此, 它为改善光电探测器性能的设计提供了一种新策略.

 © Science China Press and Springer-Verlag GmbH Germany, part of Springer Nature 2022